A Freestanding, Dissolution- and Diffusion-Limiting, Flexible Sulfur Electrode Enables High Specific Capacity at High Mass Loading

Qianyi Guo, Chao Wang, Jian Shang, Yu Yang, Chuan Xie, Yufeng Luo, Mingming Rong, Yi Pei, Yuan Gao, and Zijian Zheng*

The acquisition of stable and high-areal-capacity S cathodes over 10 mA h cm^{-2} is a critical and indispensable step to realize the high energy density configuration. However, increasing the areal capacity of S cathodes often deteriorates the specific capacity and stability due to the aggravated dissolution of S and diffusion of solvable polysulfides in the thick electrode. Herein, the design of a freestanding composite cathode that leverages 3D covalent binding sites and chemical adsorption environment to offer dissolution-limiting and diffusion-blocking functions of S species is reported. By employing this architecture, the coin cell exhibits excellent cycling stability and an exceptional specific capacity of 1444.3 mA h g^{-1} (13 mA h cm^{-2}), and the pouch cell configuration manifests a noteworthy areal capacity exceeding 11 mA h cm^{-2}. This performance is coupled with excellent flexibility, demonstrated through consecutive bending cycle tests, even at a sulfur loading of 9.00 mg cm^{-2}. This study lays the foundation for the development of flexible Li–S batteries with increased loading capacities and exceptional performance.

Q. Guo, J. Shang, Y. Yang, M. Rong, Y. Pei, Y. Gao, Z. Zheng
School of Fashion and Textiles
The Hong Kong Polytechnic University
Hong Kong SAR 999077, China
E-mail: tczzheng@polyu.edu.hk
C. Wang, C. Xie, Y. Luo, Z. Zheng
Department of Applied Biology and Chemical Technology
The Hong Kong Polytechnic University
Hong Kong SAR 999077, China
Z. Zheng
State Key Laboratory for Ultra-Precision Machining Technology
Research Institute for Smart Energy
Research Institute for Intelligent Wearable Systems
The Hong Kong Polytechnic University
Hong Kong SAR 999077, China

1. Introduction

Nowadays, a wide range of flexible and portable electronic devices impose a great necessity for developing batteries with flexibility, cost-effectiveness, and high energy density.[1] On one hand, the dominant lithium-ion batteries (LIBs) gradually reach their limit of energy density ($\approx$300 Wh kg^{-1}) due to the intercalation chemistry. Lithium–sulfur (Li–S) batteries, with ultra-high theoretical specific capacity (1672 mA h g^{-1}) and energy density (2567 Wh kg^{-1}), low cost ($\$$ 0.02 g^{-1}) and environmental benignity of S,[2] spark a hope to be the alternate next-generation energy storage devices. However, the output potential ($\approx$2.15 V) in Li–S batteries is much lower than those of LIBs ($\approx$3.7 V). As such, the fabrication of a high S-loaded electrode (>5 mg cm^{-2}) is crucial to achieving high energy density for the practically viable battery. On the other hand, the forthcoming battery systems are too heavy, bucky, and rigid to promote their portability. Hence, considerable attention has to be paid to the soaring demand for light, small, and flexible energy storage systems. However, thick electrodes suffer from the long electronic/ionic transport distance and structural instability over charge/discharge processes, which will diminish the rate performance, utilization of the active materials, and flexibility of the whole configuration.[3] Thus, a high level of S-loading electrode with excellent cyclic performance and outstanding flexibility remains a formidable challenge in Li–S batteries.

In principle, the undesirable degradation of capacity and lifetime for Li–S batteries are mainly attributed to two key behaviors of active materials during the repeated charge and discharge process: i) the inevitable dissolution of S, and ii) the uncontrolled diffusion of soluble lithium polysulfides (LiPSs). Extensive studies have been focused on alleviating the dissolution of S and controlling the diffusion of LiPSs. Widely used strategies for mitigating the dissolution of S involve the physical trapping of S inside the mesoporous carbon,[4] microporous carbon,[5] carbon fiber cloth,[6] graphene-based porous carbon,[7] carbon nanotubes,[8] etc., and chemical binding of S species with polar materials (such as metal compounds[9] and polymers with functional groups[10])

**ADVANCED
SCIENCE NEWS**

www.advancedsciencenews.com

**ADVANCED
MATERIALS**

www.advmat.de

which can largely decrease the dissolution of S and thus significantly increase the capacity of the electrode. However, these methods cannot guarantee the immobilization of S in the pores with a high mass loading and the shuttle effect remains the critical problem for the fast capacity fading away.[11] Synthesizing LiPS-adsorbing binders,[12] developing electrolytes with LiPS-blocking ability,[13] graphene-based tight interlayers,[14] and enhancing the tortuosity to prolong the diffusion length of LiPSs[15] are the common means to limit the diffusion of LiPSs. Nevertheless, these mitigation approaches often pay the cost of compromised electronic conductivity, impeded Li ion diffusion, and less reuse of the trapped active materials, which may seriously lead to poor rate performance, insufficient reaction, and irreversible loss of active materials.[16] Consequently, it is urgent to design an electrode that can overcome the critical issue of decreased specific capacity and stability when the mass loading is increased.

In this work, we report a flexible and freestanding composite S cathode (CF-SCNT-HrGO) made of carbon fibers (CFs), S-immobilized CNTs (SCNTs), and holey reduced graphene oxides (HrGOs), which offers simultaneous diffusion-limiting and dissolution-blocking functions. The CFs, SCNTs, and HrGOs interweave in the 3D space to form a unique layer-by-layer lamellar structure that is porous, highly flexible, and conductive. The surfaces of this 3D framework are chemically modified to provide ample anchoring sites to limit the dissolution of S species into the electrolyte. Meanwhile, the unique porous lamellar structure not only significantly hinders the diffusion of LiPSs but also allows efficient transport of Li ions which are particularly important for ensuring the performance of thick S electrodes. Hence, The Li/CF-SCNT-HrGO cell exhibits noteworthy capacity even without undergoing any initial activation cycles under various mass loadings. This is a sharp contrast to traditional S cathodes, where their specific capacities decline and an extended activation procedure is obligatory with increasing S loading. Importantly, the specific capacity of the electrodes improves accordingly with the increasement in mass loading, which solves the trade-off between mass loading and capacity. In this instance, the composite electrode achieves an impressive reversible specific capacity of 1444.3 mA h g^{-1}, when the areal capacity reaches 13.00 mA h cm^{-2}, with a sulfur mass loading of 9.00 mg cm^{-2}. Furthermore, exceptional cycling stability is attained, with over 430 cycles completed at 0.2 C, exhibiting a capacity degradation rate of only 0.086% per cycle. As a consequence, the CF-SCNT-HrGO cells provide an energy density of 438.8 Wh kg^{-1} (641.1 Wh L^{-1}) based on all the cell components including the current collectors, electrode materials, separator, and electrolytes. Utilizing the resilient 3D architecture of the interconnected electrode, the remarkable mechanical flexibility of the Li/CF-SCNT-HrGO pouch cell is also realized, accompanied by minimal voltage oscillations and exceptional capacity preservation in contrast to commercial Li–S cells. Moreover, robust flexibility and stability are maintained with heightened sulfur loadings of 9.00 mg cm^{-2}, even after undergoing multiple successive bending cycles. The aforementioned findings underscore the notable benefits of this electrode design for flexible Li–S batteries with elevated loading capacities and high performance.

2. Results and Discussions

2.1. Preparation and Structure of CF-SCNT-HrGO

The CF-SCNT-HrGO composite cathode was prepared by one-step vacuum infiltration of an aqueous suspension consisting of CFs, SCNTs, and HrGOs (**Figure 1**a). All materials were acid-treated rendering the surface strongly hydrophilic. The hydrophilic CNTs were further silanized with 3-(trimethoxysilyl) propyl methacrylate (KH570) and were then chemically immobilized with S via an "inverse vulcanization" process to obtain SCNTs (Figure S1, Supporting Information).[17] The three compounds were ultrasonically mixed in an aqueous solution and subsequently vacuum-filtrated to yield the CF-SCNT-HrGO composite cathode. The mass loading of S in the electrode could be easily tuned ranging from 1.51 to 9.00 mg cm^{-2} by changing the amount of filtration suspension (Figure S2, Supporting Information).

The electrode was self-assembled into a 3D interconnected framework with a unique lamellar stacking structure and hierarchical pores (Figure 1b). Each composed component has played a specific role in the composite. The microsized CFs laid on the 2D HrGO flakes and connected them into layered sheets (Figure 1c). This constructed a percolation skeleton with low resistance and robust mechanical strength, largely preventing the restocking of HrGO sheets, and promoting the electron transfers along the electrode (Figure 1c; and Figure S3, Supporting Information). The nanosized SCNTs were dispersed on the layered sheets and interconnected in the 3D space (Figure 1d,e). The change in the surface chemistry could be reflected by the loss of the dispersion ability of silanized CNT in acetone after coating S (Figure S4, Supporting Information).[18] Figure 1f showed the transmission electron microscope (TEM) image of HrGO with a holey structure. The HrGO nanosheets with O and N-containing groups enabled a strong interfacial adhesion to bind SCNT and CF into freestanding integrity.[19]

Taking advantage of the self-assembly process, the gaps naturally formed between neighboring layers offered sufficient space for efficiently trapping electrolytes and buffering the volume change. The interspace allowed the neighboring layers to slide over each other in the horizon direction to dissipate the tensile stress produced during mechanical deformation. As a proof of concept, we bent the CF-SCNT-HrGO composite electrode at a small radius of 2.5 mm. No apparent change in the electrical resistance or morphology was observed after 10 000 bending cycles (Figure S5, Supporting Information). In comparison, the electrode constructed by a single component (CF, SCNT, or HrGO) exhibited dissatisfactory mechanical features to maintain a freestanding film. The electrode made of CF or SCNT lacked adhesion to form a compact film, while that made of HrGO was very brittle and was easy to crack into small pieces (Figure 1g).

2.2. Dual Dissolution-Limiting and Diffusion-Blocking Mechanism

Figure 2 presented the design principle of the dissolution-limiting function and relevant characterization of the

ADVANCED
SCIENCE NEWS
www.advancedsciencenews.com
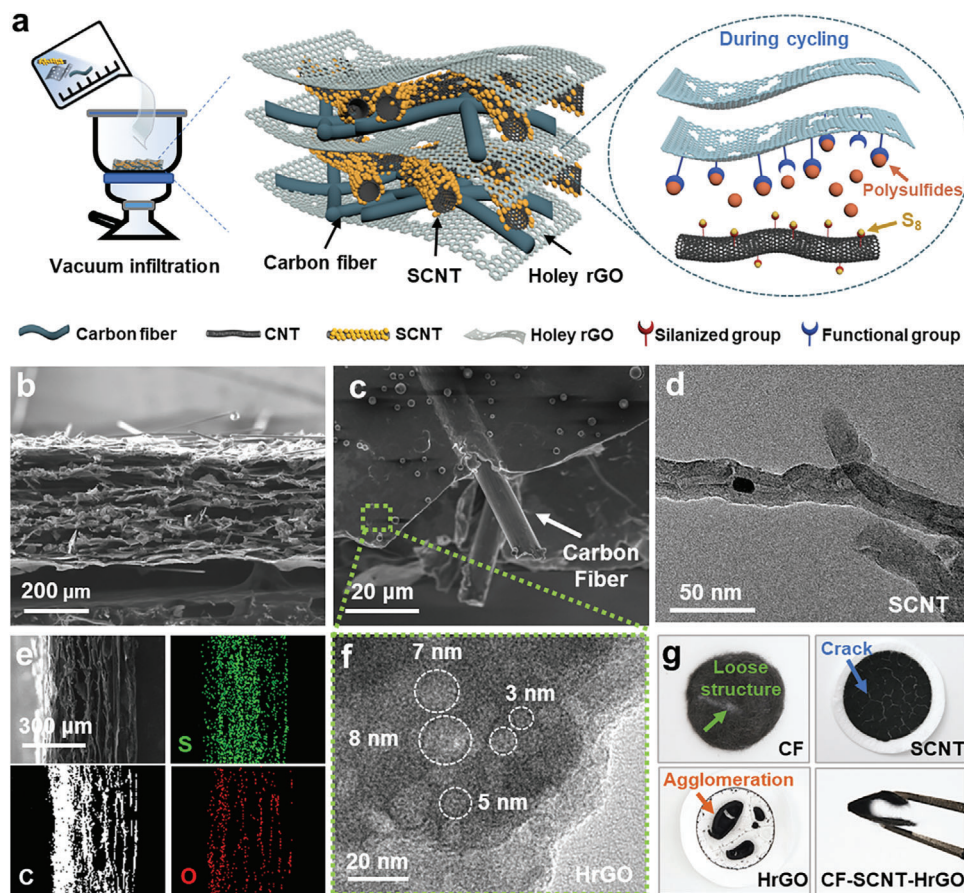
ADVANCED
MATERIALS
www.advmat.de

Figure 1. Preparation and characterizations of the CF-SCNT-HrGO composite electrode. a) Schematic illustration of the preparation and design principle of CF-SCNT-HrGO electrode. b) The cross-section SEM image of the CF-SCNT-HrGO electrode. c) The SEM image of CF compound. d) The TEM image of SCNT and e) the element mappings (EDS) of CF-SCNT-HrGO electrode. f) The TEM image of the HrGO compound. g) The digital images of pure CF, SCNT, HrGO, and CF-SCNT-HrGO electrodes.

CF-SCNT-HrGO composite electrode. The dissolution-limiting feature was mainly achieved by the covalent bonding of S with a silanized CNT host, which can efficiently hinder the dissolution of S species into the electrolyte (Figure 2a). The chemical bonding can be verified by Fourier-transform infrared spectroscopy (FTIR) and X-ray photoelectron spectroscopy (XPS). The silanized CNT showed typical FTIR adsorption peaks of Si—O—C (1091 cm^{-1}) and C=C (1632 cm^{-1}).[20] After the S immobilization, the stretching vibration band of C=C disappeared (Figure 2b).

The survey spectra of CNT, silanized CNT, and SCNT were shown in Figure 2c. The signals of elemental C, O, and Si in the silanized CNT gave additional evidence of the grafting of silane on CNT. The relative atomic content of C, O, and Si elements in silanized CNT were determined to be 87.34%, 11.54%, and 1.12%, respectively. These peaks remained in the XPS spectra of SCNT with an additional peak of element S, suggesting the stable anchor of the functional groups on CNT. The high-resolution XPS spectra of Si 2p, C 1s, and S 2p were performed to study the chemical structure of SCNT. The high-resolution Si 2p XPS spectrum was divided into the peaks of Si—O—C (102.9 eV) and Si—O (104.7 eV), ascribing to the hydrolysis reaction between 3-(methacryloyloxy) propyl trimethoxysilane solu-

tion (KH570) and CNT (Figure S6, Supporting Information).[21] The high-resolution C 1s XPS spectrum was fitted into five peaks, corresponding to the C—S (283.9 eV), C—C (284.6 eV), C—O (285.6 eV), C=O (286.8 eV), —COOR (288.9 eV) bond, respectively (Figure 2d).[22] The presence of the covalent C—S bond accounted for the polymerization between S and silanized CNT, which was also further demonstrated by the high-resolution S 2p XPS spectrum (Figure 2e). The high-resolution S 2p XPS spectrum showed two peaks centered at 163.8 eV (S 2p$_{3/2}$) and 165.1 eV (S 2p$_{1/2}$), respectively, confirming the existence of C—S and S—S in SCNT. In addition, the peak at 168.5 eV was indexed to the sulfate species (SO$_x$).[23]

The diffusion-blocking process and relevant characterizations were shown in **Figure 3**. The efficient diffusion-blocking feature of CF-SCNT-HrGO was evidenced by the strong intercalation between polysulfides and CF-SCNT-HrGO after Li$_2$S$_6$ adsorption, as revealed in the XPS spectrum (Figure S7, Supporting Information). The diffusion-blocking function was mainly provided by i) the abundant O, N-containing functional groups of HrGO nanosheets and ii) the physical blocking of the horizontally stacked structure of composite electrodes (Figure 3a). The nanoscale holey structure and O, N-containing groups of HrGO enabled a strong capillary and binding force to limit the
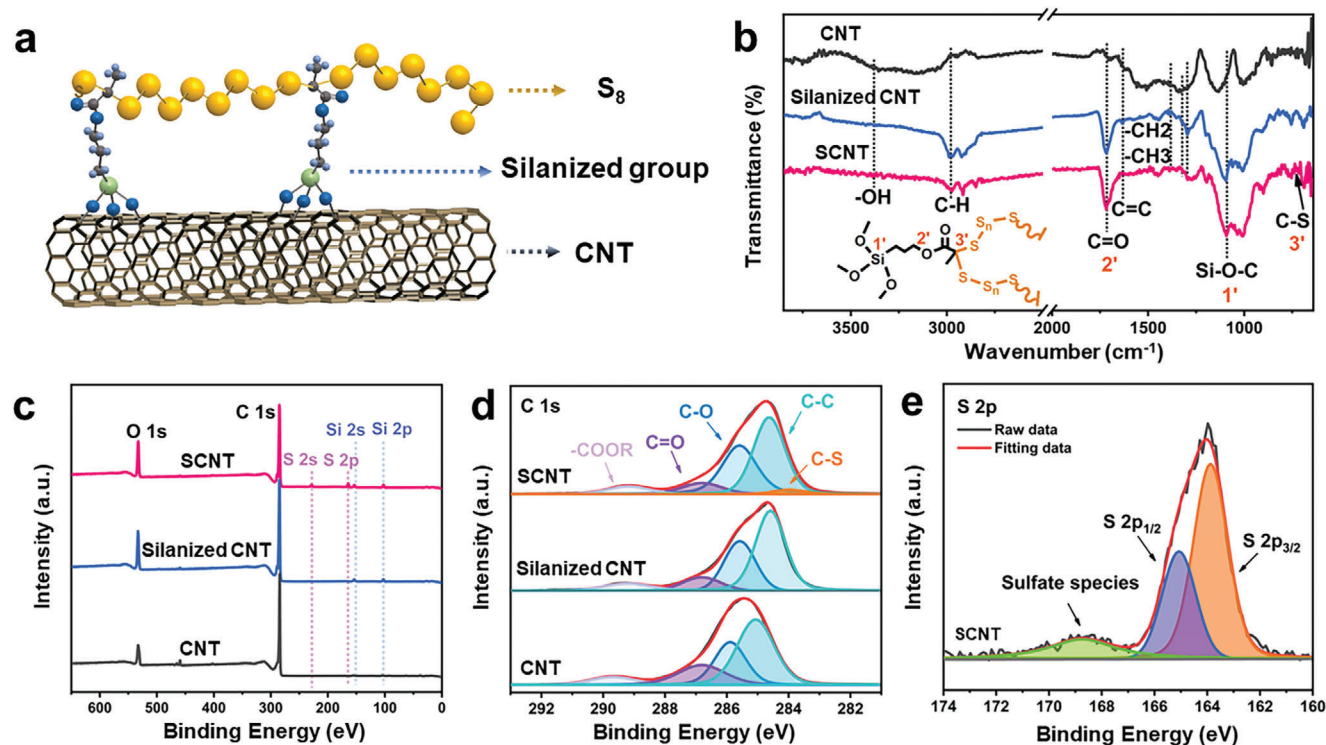
2400041 (3 of 11)

Figure 2. Designing principle of the dissolution-limiting function and relevant characterization of CF-SCNT-HrGO composite electrode. a) Schematic illustration of the dissolution-limiting process in CF-SCNT-HrGO electrodes. b) The FTIR spectra of CNT, silanized CNT, and SCNT. c) The XPS survey spectra and d) the high-resolution C 1s spectrum of CNT, silanized CNT, and SCNT. e) The high-resolution S 2p spectrum of SCNT.

dissolution of polysulfides.[24] The Brunauer–Emmett–Teller (BET) surface area analysis of HrGO showed that the specific surface area was 400.56 m² g⁻¹ and the average pore size was 3.30 nm (Figure S8 and Table S1, Supporting Information). Thus, the composite electrode presented a strong ability to physisorb polysulfides.[25] The trapped polysulfides were further chemically immobilized by doped N atom and oxygen functional groups (e.g., from —OH) of HrGO via dipole–dipole interaction.[26] As identified by the XPS analysis (Figure 3b,c; and Figure S9, Supporting Information), the oxygen-containing groups of GO were

partially reserved in HrGO, while the N heteroatoms were incorporated after the hydrazine reduction process.[27] As shown in Figure 3c, the dominated doping of electron-rich pyridinic N (399.7 eV) and pyrrolic N (402.5 eV) in HrGO tended to form strong binding with LiPSs.[28] The polysulfide adsorption ability of HrGO was also demonstrated by the density functional theory (DFT) theoretical calculation, showing stronger adsorption energy of HrGO with different lithium polysulfides compared with that of rGO (Figures S10 and S11, Supporting Information). Raman and X-ray diffraction (XRD) spectroscopies
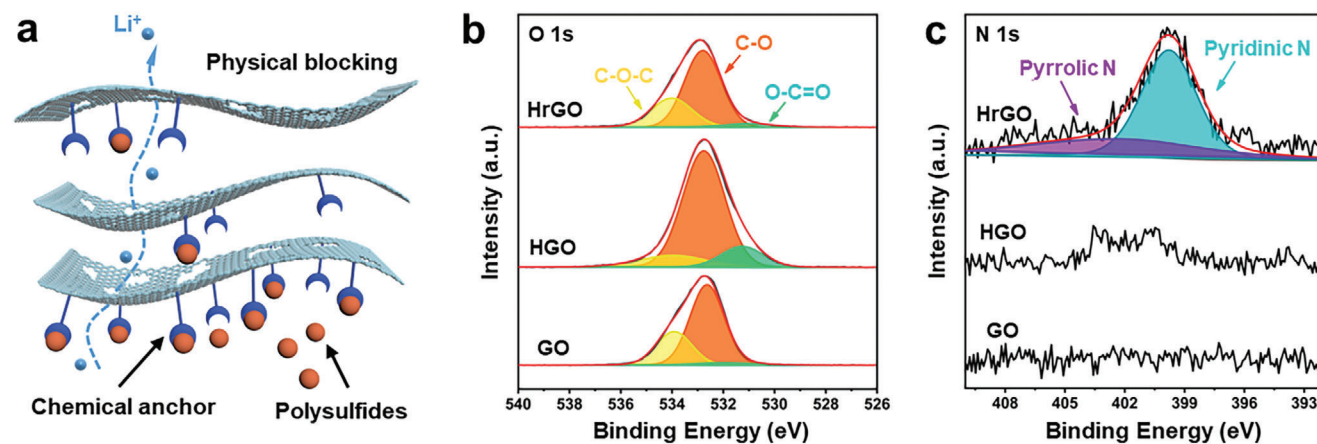

Figure 3. The diffusion-blocking process and relevant characterizations of CF-SCNT-HrGO composite electrodes. a) Schematic illustration of the diffusion-blocking process in CF-SCNT-HrGO composite electrodes. The XPS high-resolution b) O 1s, and c) N 1s spectrum of GO, HGO, and HrGO.
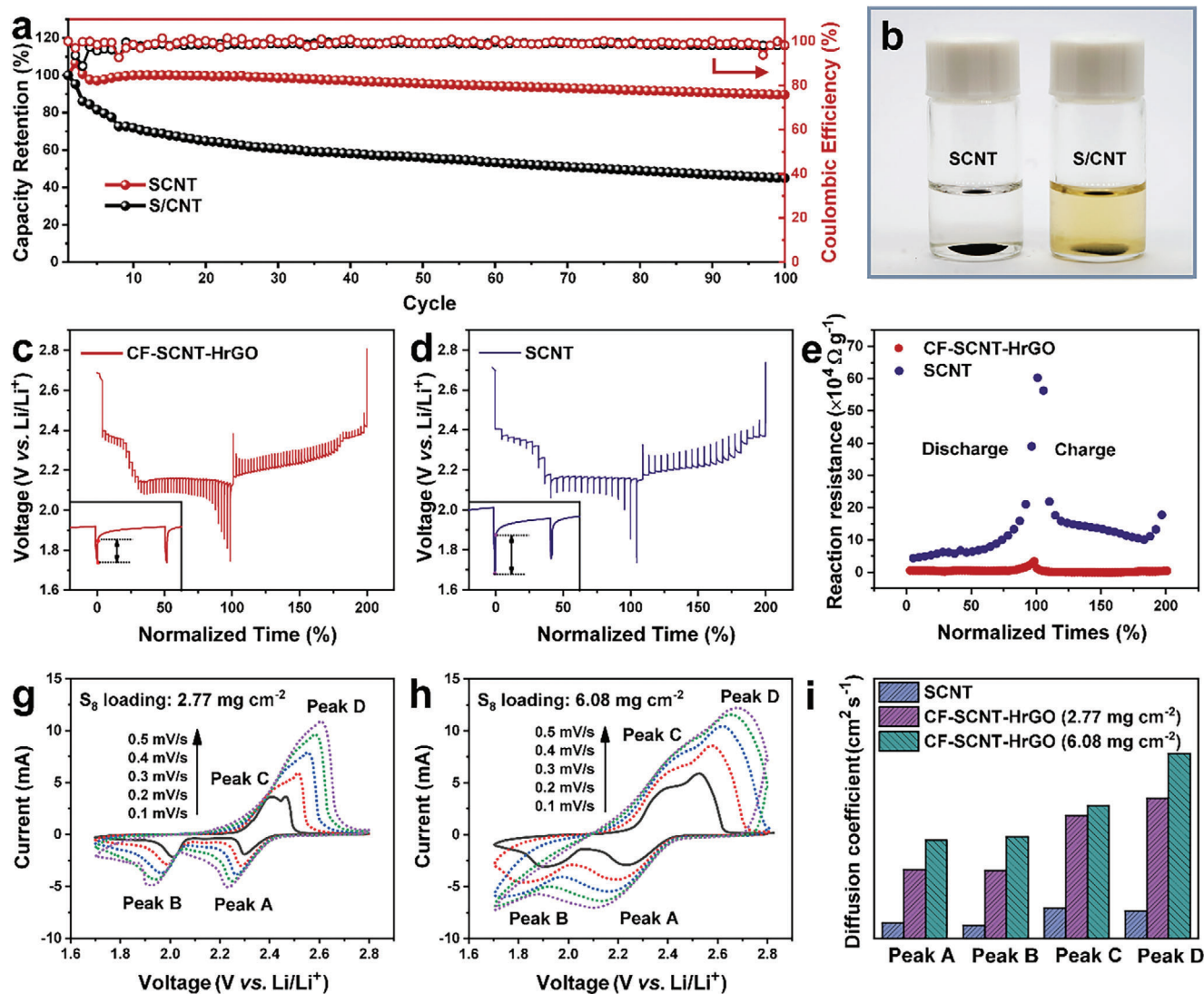
ADVANCED
SCIENCE NEWS

www.advancedsciencenews.com

ADVANCED
MATERIALS

www.advmat.de

Figure 4. The electrochemical properties of CF-SCNT-HrGO composite electrodes with dissolution-limiting and diffusion-blocking functions. a) The capacity performance of SCNT and S/CNT electrodes at a current rate of 0.1C was fabricated by the blade-casting method (S: 2.0 mg cm^{-2}). b) The solvability of SCNT and S/CNT in the electrolyte after discharge to 2.1 V. The GITT plots of c) CF-SCNT-HrGO and d) SCNT electrode at a current rate of 0.05 C-rate (S: 4.5 mg cm^{-2}). Insets showed the voltage difference. e) The calculated reaction resistances of CF-SCNT-HrGO and SCNT electrodes (S: 4.5 mg cm^{-2}) concerning normalized discharge-charge time. The CV profiles of the composite electrodes with different mass loading of g) 2.77 mg cm^{-2} and h) 6.08 mg cm^{-2} at a series of scan rates (0.1–0.5 mV s^{-1}). i) The calculated Li-ion diffusion coefficients of composite electrodes with different mass loading, with the SCNT (S: 2.0 mg cm^{-2}) electrodes as reference.

were used to further identify the chemical structure of HrGO. The HrGO showed a high degree of disorder, suggested by the relatively high I_D/I_G ratio of 1.14 in Raman spectra (Figure S12, Supporting Information) and oxygen content of 14.5% calculated from XPS spectra.[29] Besides, the XRD peaks of HrGO matched well with the typical amorphous structure of rGO (Figure S13, Supporting Information).[30] The multilayer stacking structure of the CF-SCNT-HrGO composite efficiently enlarged the outward diffusion distance to suppress the fast diffusion of soluble S species. The dense surface layers acted as the physical blocking to further mitigate the diffusion of LiPSs (Figure S14, Supporting Information). The vertical pores and voids provided efficient pathways for Li ions to quickly get access to the inner parts of

the composite electrode, which is particularly important for thick S electrodes. The electrolyte exhibited a 0° contact angle on the composite electrode, and upon contact, it was rapidly absorbed into the composite electrode.

The electrochemical properties of the CF-SCNT-HrGO composite were evaluated to investigate the effect of combining dissolution-limiting and diffusion-blocking functions via surface functionalization and architecture design (**Figure 4**). To verify the dissolution-limiting behavior of SCNTs, we first prepared a SCNTs-only electrode and an electrode made of physically mixed S and CNTs (noted as S/CNT) as a comparison. As shown in Figure 4a, the cycling stability of SCNT was significantly superior to that of the mixed S and CNTs. The solubility test also

ADVANCED
SCIENCE NEWS

www.advancedsciencenews.com

ADVANCED
MATERIALS

www.advmat.de

demonstrated the robust anchoring of S on SCNT (Figure 4b). The diffusion-blocking function of the composite electrode was examined by cyclic voltammetry (CV) and galvanostatic intermittent titration technique (GITT) measurements. The areal S loading in the electrode was set to be as high as 4.5 mg cm^{-2}, aiming to evaluate the performance of thick electrodes. The SCNT-only electrode was tested for comparison (Figure S15, Supporting Information). The composite electrode showed representative reduction peaks at 2.23 and 1.94 V, attributing to the conversion of S to long-chain LiPSs (Li$_2$S$_n$, $3 \leq n \leq 8$) and the formation of insoluble Li$_2$S$_2$/Li$_2$S, respectively. The corresponding oxidation peak at 2.39 and 2.50 V indicated the oxidation of Li$_2$S to S$_8$. In comparison to the SCNT-only electrode, the peak positions of CF-SCNT-HrGO presented an upshift in the reduction process and a downshift in the oxidation, but higher intensities. The above features reflected a low polarization and fast redox reaction of CF-SCNT-HrGO at such a high S loading. The polarization of the electrode was quantified by the reaction resistances examined by GITT. The internal resistances (ΔR) were calculated based on the applied current and the voltage difference between the closed-circuit-voltage (CCV) and the quasiopen-circuit-voltage (QOCV).[31] As shown in the inset images of Figure 4c,d, the reaction resistances of CF-SCNT-HrGO during both the discharge and charge processes were much lower than that of the SCNT electrode, which revealed improved electrochemical kinetics (Figure 4e). In addition, the charge and discharge plateaus of composite electrodes showed a much larger capacity compared with the SCNT electrodes, demonstrating a high efficiency of conversion reaction (Figure S16, Supporting Information).[32]

To further determine the reaction kinetics of thick electrodes, the CV of composite electrodes with different S loading was performed with the scan rate varied from 0.1 to 0.5 mV s^{-1}. In the CV profiles, the cathodic peaks at 2.30 and 2.00 V, and the anodic peaks at 2.41 and 2.46 V, were labeled as peaks A to D (Figure 4g,h). Based on the Randles–Sevcik equation, the Li-ion diffusion coefficients at each peak were determined by the slope of peak current (I_p) versus the square root of the sweeping rate (v$^{0.5}$).[33] The high Li-ion diffusion was expected to accelerate the kinetic of corresponding conversion processes. The CF-SCNT-HrGO composite electrode exhibited improved Li-ion diffusion at all four peaks with the increasing S loading, as shown in Figure 4i; and Figure S17 (Supporting Information). The improved Li-ion conductivities in high-loaded composite electrodes confirmed their outstanding polysulfide conversion kinetics that benefited the capacity performance.

2.3. Coin Cell Performance

The electrochemical performance of CF-SCNT-HrGO composite electrodes with a series of mass loadings (1.51, 3.45, 4.82, and 9.00 mg cm^{-2}) was evaluated by coin cells (**Figure 5**). When the mass loading was increased from 1.51 to 9.00 mg cm^{-2}, the areal capacity rose approximately linearly from 1.68 to 13.00 mA h cm^{-2} (Figure 5a; and Table S2, Supporting Information). In accordance, the corresponding initial specific capacity increased by 30.6%, from 1105.8 to 1444.3 mA h g^{-1}. The voltage profiles displayed stable voltage plateaus, which were consistent with the typical charge and discharge processes (Figures S18 and S19,

Supporting Information). The reversible capacity of 1.49, 4.06, 5.17, and 11.35 mA h cm^{-2} was achieved after cycling 100 cycles at the loading of 1.51, 2.45, 4.82, and 9.00 mg cm^{-2}, respectively (Figure 5b). High capacities of 1273.5, 990.6, 818.9, 702.2, and 520.5 mA h g^{-1} were also obtained in the composite electrode under the current rate of 0.1, 0.2, 0.5, 1.0, and 2.0 C, respectively (Figure S20, Supporting Information). The electrochemical polarization of electrodes was relatively low ($\approx$0.2 V) at a relatively high loading of S ($>$3 mg cm^{-2}). With the dual dissolution-limiting and diffusion-blocking functions, the high S-loaded CF-SCNT-HrGO electrode showed outstanding capacity retention upon cycling. The long-term cycling performance of the CF-SCNT-HrGO composite electrode at 0.2 C was investigated. The cathode delivered a reversible specific capacity of 1293.0 mA h g^{-1} (7.76 mA h cm^{-2}) without the initial activation cycle (Figure S21, Supporting Information). A capacity of 812.6 mA h g^{-1} (4.88 mA h cm^{-2}) was maintained after 430 cycles, equivalent to a capacity fading rate of 0.086% per cycle. While the SCNT electrode fabricated with such high mass loading could only retain an initial capacity of 724 mA h g^{-1} (4.35 mA h cm^{-2}) and encountered a sudden failure of the battery after 100 cycles. A clean surface of the CF-SCNT-HrGO composite electrode was observed in the disassembled cell after the cycling test, illustrating the efficient suppression of the dissolution of LiPSs compared to the SCNT electrode (Figure S22, Supporting Information). There was no obvious Li dendrites growth on the anode side (Figure S23, Supporting Information).

Very importantly, we found that the unique advantages of ultrahigh S-loaded CF-SCNT-HrGO could be explained by its elastic structure. Because of the unique lamellar layered structure, the CF-SCNT-HrGO electrode was highly compressive upon pressing. In the coin cell setup, due to the fixed space of the cell, the applied pressure on the electrode increased when the mass loading (so as the thickness) of the electrode increased. Indeed, we found that when the mass loading of the CF-SCNT-HrGO electrode increased, the electrode was compressed gradually, leading to a denser structure of the electrode. Therefore, the electrochemical impedance of the CF-SCNT-HrGO electrode decreased when the mass loading increased (Figure 5c). This phenomenon explained the increased specific capacity at a higher mass loading that we discussed in Figure 5a,b. To further prove this observation, we fixed the mass loading of the CF-SCNT-HrGO electrode and then changed the thickness of the stainless steel slab to tune the compression status of the electrode. The CF-SCNT-HrGO electrode (S: 9.00 mg cm^{-2}) was compressed to a denser and thinner film at higher pressure (Figures S24 and S25, Supporting Information). As shown in Figure 5d,e, higher compression resulted in the observation of enhanced capacity, reaching up to 13 mA h cm^{-2}, and a reduction in charge transfer resistance to as low as 60 ohms.

Normally, the specific capacity of the electrode was adversely affected by the enhancement of mass loading. It was difficult for thick electrodes ($>$5 mg cm^{-2}) to maintain a similar specific capacity and cycling stability to those of thin electrodes. Consequently, the corresponding areal capacities and gravimetric energy densities of Li–S batteries tended to largely decrease with increasing S loading, as summarized in Figure 5f; and Table S3 (Supporting Information). For one reason, the elongated ion diffusion distance and poor electronic conducting network caused sluggish reaction conversion in the thick electrodes.
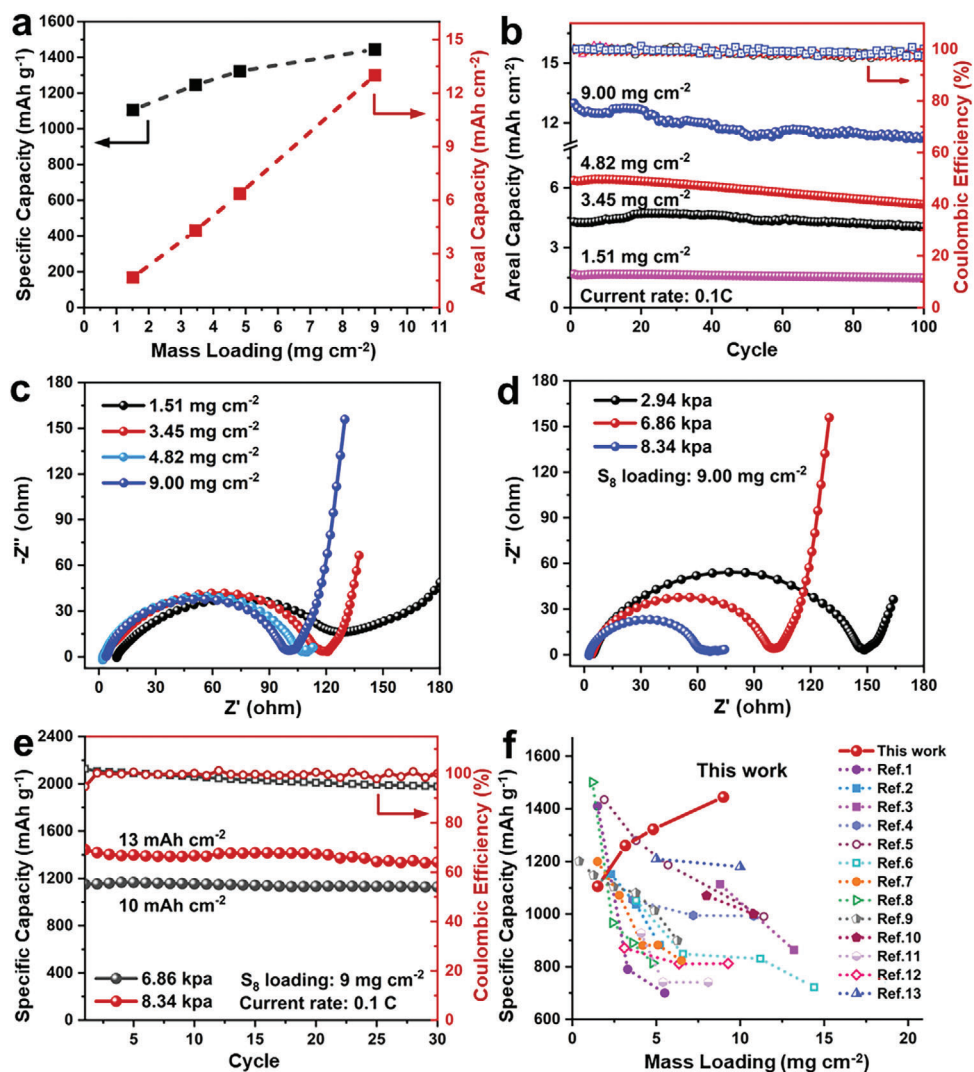
Figure 5. Electrochemical performances of cells using CF-SCNT-HrGO composite electrodes with a series mass gradient. a) The capacity-mass loading curves of CF-CNT-HrGO composite electrodes (based on initial capacity). b) Cycling performance of CF-CNT-HrGO composite electrodes under different mass loading at the current rate of 0.1C. c) The Nyquist plots of the composite electrodes with different mass loading before cycling. d) The Nyquist plots and e) capacity performance of composite electrodes (S loading: 9.00 mg cm^{-2}) fabricated with different pressures by tuning the thickness of the stainless steel in the coin cells. f) The specific capacity-mass loading curves of this work compared with other reports.

The interfacial problems such as Li dendrite growth and sluggish conversion of insulated electrochemical species were intensified accordingly. For other reasons, the poor mechanical properties of thick electrodes not only caused poor electronic contact by delaminating the electroactive species from the electrode but also greatly limited their stress tolerance upon deformations. Benefiting from the surface modification and structural design, the 3D porous CF-SCNT-HrGO composite electrode constructed by 1D or 2D carbon materials exhibited good electrochemical and mechanical properties. It endowed the composite electrode with improved robustness and flexibility, more active surface area, sufficient pores for ionic conductivity, and an interconnected conductive skeleton to solve the above-mentioned issues. As a result, it achieved a high specific capacity of 1444.3 mA h g^{-1}, a gravimetric energy density of 438.8 Wh kg^{-1}, and a volumetric energy density of 641.1 Wh L^{-1} (based on all cell components) at a high S

loading of 9.00 mg cm^{-2} (Figure 5f; and Table S4, Supporting Information). The construction of CF-SCNT-HrGO composite electrodes offered a promising approach to address the trade-off between mass loading and high capacity/energy density for Li–S batteries.

2.4. Pouch Cell Configuration

Given the remarkable flexibility and excellent electrochemical stability of the CF-SCNT-HrGO electrode, the pouch-type full-cell configuration was assembled to further estimate its practical performance and mechanical flexibility. The commercial S electrodes and the CF-SCNT-HrGO electrodes with varying mass loading were selected to pair with the 100 μm thick lithium metal anode. Following the first activation cycle, a bending test was

ADVANCED
SCIENCE NEWS

www.advancedsciencenews.com
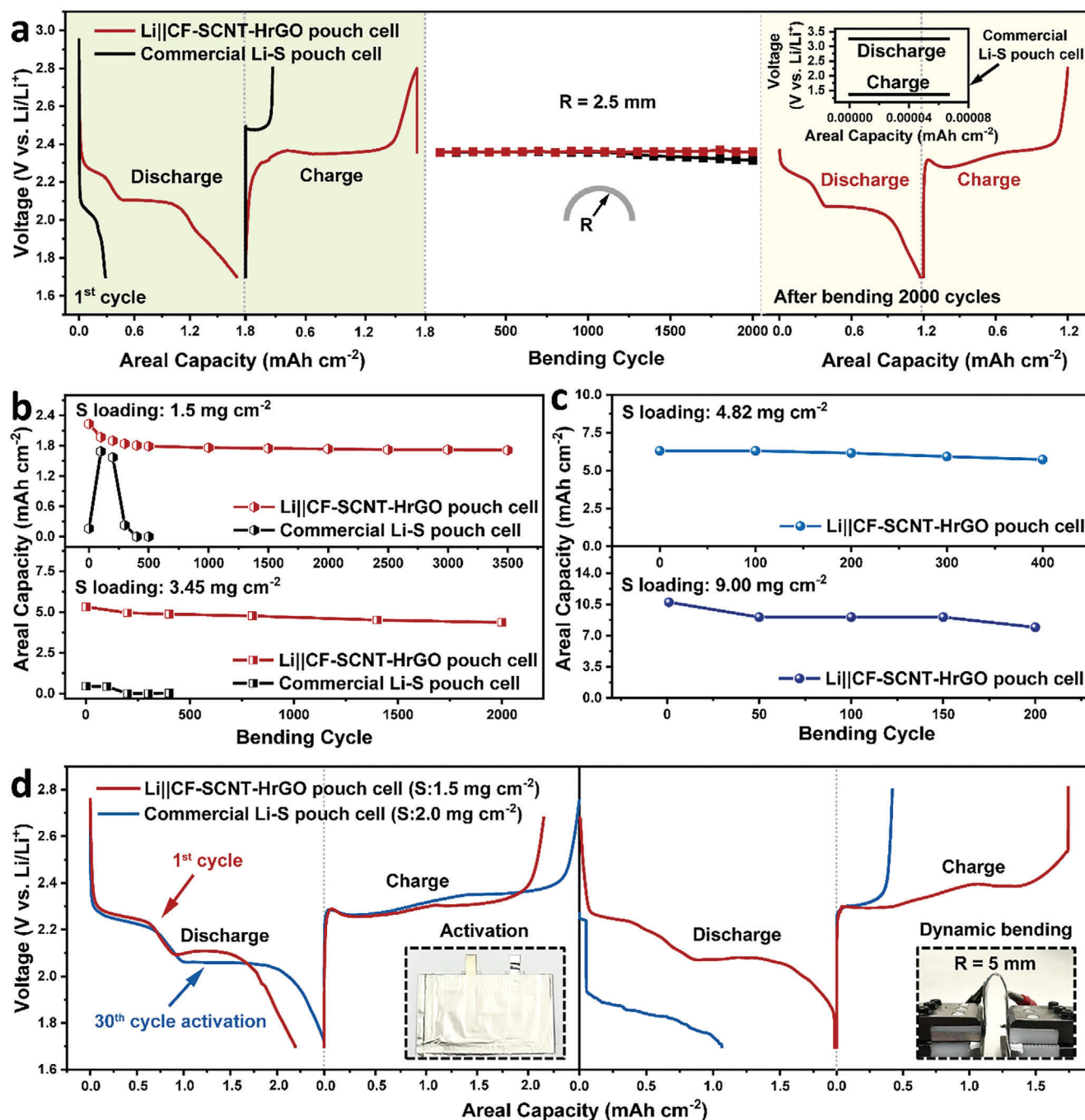
ADVANCED
MATERIALS

www.advmat.de

Figure 6. Electrochemical performances of pouch cell configuration at 0.05 C. a) OCV stability test of the assembled full cells with CF-SCNT-HrGO (1.5 mg cm^{-2}) and S (2.0 mg cm^{-2}) cathodes during 2000 bending times at a radius of 2.5 mm. Inset was the charge and discharge profile of the commercial Li–S cell. b) Consecutive bending test of the full cells with CF-SCNT-HrGO (1.5 and 3.45 mg cm^{-2}) and S (2.0 and 4.0 mg cm^{-2}) cathodes. c) Consecutive bending test of the full cells with CF-SCNT-HrGO (4.82 and 9.00 mg cm^{-2}) cathodes. d) Dynamic bending test of the full cells at a bending radius of 5 mm with CF-SCNT-HrGO (1.5 mg cm^{-2}) and S (2.0 mg cm^{-2}) cathodes after fully activated. Insets were digital photos of the cells before activation and during dynamic bending.

conducted on the pouch cells containing CF-SCNT-HrGO and the commercial S electrodes with a mass loading of 1.5 and 2.0 mg cm^{-2}, respectively. Illustrated in **Figure 6a**, when subjected to a bending radius of 2.5 mm, the open circuit voltage (OCV) of the Li/CF-SCNT-HrGO cell exhibited robust stability,

with only minor voltage fluctuations of less than 10 mV over 2000 bending cycles. In contrast, the OCV of the commercial Li–S cell experienced a slight decrease from 2.36 to 2.31 V. After bending 2000 cycles, the Li/CF-SCNT-HrGO cell successfully maintained stable charge and discharge processes, retaining 70% of its

**ADVANCED
SCIENCE NEWS**

www.advancedsciencenews.com

**ADVANCED
MATERIALS**

www.advmat.de

initial capacity. In contrast, the commercial Li–S cell experienced failure, yielding almost no capacity. The possible reason might be that during the bending of the commercial Li–S cell, fractures and delamination emerged on the S–Al electrode.[34] This subsequently resulted in the failure of the barely activated commercial Li–S cell. Thanks to the elastic 3D architecture of the CF-SCNT-HrGO electrode, the Li/CF-SCNT-HrGO cell exhibited the ability to withstand shear forces and delamination while undergoing bending cycles. Beyond its contribution to improved electrochemical performance, these distinctive 3D structures also confer notable mechanical flexibility of the Li/CF-SCNT-HrGO cell.

A continuous bending test was similarly conducted on the pouch cells (as depicted in Figure 6b,c). In the case of the Li/CF-SCNT-HrGO cell, featuring an S loading of 1.5 mg cm^{-2}, even after undergoing 3500 consecutive bending cycles at a radius of 2.5 mm, the pouch cell managed to uphold more than 77% of its initial capacity, and no discernible instances of cell failure were detected (the voltage files of each cycle were shown in Figure S26, Supporting Information). On the contrary, the commercial Li–S cell, with an S loading of 2.0 mg cm^{-2}, encountered rapid failure within 500 cycles. For a more elevated S mass loading in both the Li/CF-SCNT-HrGO and commercial Li–S cells, at 3.45 and 4.0 mg cm^{-2}, respectively, the Li/CF-SCNT-HrGO cell maintained a consistent cycling regimen even after 2000 bending cycles, retaining an areal capacity of 4.33 mA h cm^{-2} (equivalent to 81% of the initial capacity). The bending assessment was also performed on the fully activated (after 30 cycles) commercial Li–S cell with an S loading of 4.0 mg cm^{-2}. However, the cell experienced failure after undergoing 500 bending cycles, primarily attributed to the rigid and thick S electrode (As shown in Figures S27 and S28, Supporting Information). The sustained bending examination of Li/CF-SCNT-HrGO cells, featuring an ultrahigh S loading of 4.82 and 9.00 mg cm^{-2}, was also conducted (as depicted in Figure 6c). These cells demonstrated remarkably steady charge and discharge processes even after 400 and 200 bending cycles, respectively. They retained a substantial capacity, with 90% and 74% of the initial capacity, respectively. Due to its distinctive lamellar layered structure, the profoundly resilient and elastic CF-SCNT-HrGO electrode exhibited the ability to withstand shear forces during the bending assessment. This capability led to the attainment of both consistent cycling performance and exceptional flexibility, even at such elevated S loadings (up to 9.00 mg cm^{-2}). The degradation in capacity is likely attributed to the reformation of the disrupted solid electrolyte interface resulting from the bending process.[35]

A dynamic bending assessment was carried out while the pouch cells were in the fully activated state, featuring mass loadings of 1.5 and 2.0 mg cm^{-2}, respectively. An important observation was that while the commercial Li–S cell required 30 cycles to become fully activated, the Li/CF-SCNT-HrGO cell displayed significant capacity even without any activation cycles at all mass loadings. As shown in Figure 6d, the Li/CF-SCNT-HrGO cell displayed remarkable stability, maintaining high-capacity retention of 87% and excellent reversibility throughout the charge and discharge processes. Conversely, the commercial Li–S cell experienced an abrupt voltage drop in the discharge phase and exhibited low-capacity reversibility during the charging state. After the dynamic bending test, the electrochemical impedance spectroscopy (EIS) of the pouch cells was conducted (Figure S29, Supporting Information). While the R_{ct} of the Li/CF-SCNT-HrGO cell remained stable, the commercial Li–S cell exhibited a significant increase in its R_{ct} value. The above results further demonstrated that the Li/CF-SCNT-HrGO cell had a notably steadier, interlinked, and flexible structure when compared to the conventional Li–S cell.

To illustrate the advantage of such flexible, high-loading, and high-performance pouch cells in achieving high-energy practical batteries, we further compared the calculated energy density of Li/CF-SCNT-HrGO cell with the commercial Li–S pouch cell by using a high areal capacity of >10 mAh cm^{-2}. The whole cell mass including S cathode, Li metal anode, additive materials, separator, and electrolyte, was considered to evaluate the potential specific energy of batteries. As proof of our concept, the CF-SCNT-HrGO thick electrode configuration could achieve a notable improvement of the gravimetric energy density of 46.96% by minimizing the inactive components (e.g., current collectors, binders, and conductive agents) at the cell level (Table S5, Supporting Information).

3. Conclusions

In conclusion, we have reported a 3D dual-functional CF-SCNT-HrGO composite electrode that limited the dissolution of S and blocked the diffusion of LiPSs combined with notable flexibility. Intriguingly, the CF-SCNT-HrGO electrode showed an unprecedented unique property, i.e., improved specific capacity with increasing S loading by taking the compressibility of the composite structure. In this case, the composite electrode delivered a high reversible specific capacity of 1444.3 mA h g^{-1} when its areal capacity was as high as 13.00 mA h cm^{-2} at the S mass loading of 9.00 mg cm^{-2}. Additionally, outstanding cycling stability is attained, surpassing 430 cycles at 0.2 C, with a capacity degradation rate of only 0.086% per cycle. Moreover, The Li/CF-SCNT-HrGO cell displayed significant capacity even without any activation cycles at all mass loadings. This stands in stark contrast to conventional S cathodes, wherein their specific capacities decreased and a long activation process was needed as the S loading increased. Thanks to the elastic 3D structure of the interconnected electrode, the Li/CF-SCNT-HrGO pouch cell exhibited improved electrochemical performance and notable mechanical flexibility. The Li/CF-SCNT-HrGO pouch cell exhibited only minor voltage fluctuations and high-capacity retention (81% of the initial capacity at S loading of 3.45 mg cm^{-2}) after 2000 bending cycles. Robust flexibility and stability were also attained even at elevated S loadings of 9.00 mg cm^{-2} after undergoing numerous consecutive bending cycles. The freestanding nature of the CF-SCNT-HrGO composite electrode, along with its ease of handling, makes it suitable for processing through a scalable, roll-to-roll approach for the assembly of flexible Li–S batteries with high energy density.

Supporting Information

Supporting Information is available from the Wiley Online Library or from the author.

**ADVANCED
SCIENCE NEWS**

www.advancedsciencenews.com

**ADVANCED
MATERIALS**

www.advmat.de

[1] a) G. Zhou, F. Li, H.-M. Cheng, *Energy Environ. Sci.* **2014**, *7*, 1307; b) H. J. Peng, J. Q. Huang, Q. Zhang, *Chem. Soc. Rev.* **2017**, *46*, 5237.

[2] a) P. G. Bruce, S. A. Freunberger, L. J. Hardwick, J.-M. Tarascon, *Nat. Mater.* **2011**, *11*, 19; b) R. Fang, S. Zhao, Z. Sun, D.-W. Wang, H.-M. Cheng, F. Li, *Adv. Mater.* **2017**, *29*, 1606823; c) A. Manthiram, Y. Fu, S. H. Chung, C. Zu, Y. S. Su, *Chem. Rev.* **2014**, *114*, 11751.

[3] H.-J. Peng, J.-Q. Huang, X.-B. Cheng, Q. Zhang, *Adv. Energy Mater.* **2017**, *7*, 1700260.

[4] a) M. Wang, H. Zhang, W. Zhou, X. Yang, X. Li, H. Zhang, *J. Mater. Chem. A* **2016**, *4*, 1653; b) Z. Li, J. T. Zhang, Y. M. Chen, J. Li, X. W. Lou, *Nat. Commun.* **2015**, *6*, 8850.

[5] S. Xin, L. Gu, N.-H. Zhao, Y.-X. Yin, L.-J. Zhou, Y.-G. Guo, L.-J. Wan, *J. Am. Chem. Soc.* **2012**, *134*, 18510.

[6] R. Elazari, G. Salitra, A. Garsuch, A. Panchenko, D. Aurbach, *Adv. Mater.* **2011**, *23*, 5641.

[7] X. Jia, C. Zhang, J. Liu, W. Lv, D.-W. Wang, Y. Tao, Z. Li, X. Zheng, J.-S. Yu, Q.-H. Yang, *Nanoscale* **2016**, *8*, 4447.

[8] S. Luo, W. Sun, J. Ke, Y. Wang, S. Liu, X. Hong, Y. Li, Y. Chen, W. Xie, C. Zheng, *Nanoscale* **2018**, *10*, 22601.

[9] a) Y. Zhong, D. Chao, S. Deng, J. Zhan, R. Fang, Y. Xia, Y. Wang, X. Wang, X. Xia, J. Tu, *Adv. Funct. Mater.* **2018**, *28*, 1706391; b) C. Zhao, G. L. Xu, Z. Yu, L. Zhang, I. Hwang, Y. X. Mo, Y. Ren, L. Cheng, C. J. Sun, Y. Ren, X. Zuo, J. T. Li, S. G. Sun, K. Amine, T. Zhao, *Nat. Nanotechnol.* **2021**, *16*, 166.

[10] F. Wu, S. Chen, V. Srot, Y. Huang, S. K. Sinha, P. A. van Aken, J. Maier, Y. Yu, *Adv. Mater.* **2018**, *30*, 1706643.

[11] H. Yao, K. Yan, W. Li, G. Zheng, D. Kong, Z. W. Seh, V. K. Narasimhan, Z. Liang, Y. Cui, *Energy Environ. Sci.* **2014**, *7*, 3381.

[12] a) W. Chen, T. Lei, T. Qian, W. Lv, W. He, C. Wu, X. Liu, J. Liu, B. Chen, C. Yan, J. Xiong, *Adv. Energy Mater.* **2018**, *8*, 1702889; b) S. Tu, X. Chen, X. Zhao, M. Cheng, P. Xiong, Y. He, Q. Zhang, Y. Xu, *Adv. Mater.* **2018**, *30*, 1804581; c) W. Chen, T. Qian, J. Xiong, N. Xu, X. Liu, J. Liu, J. Zhou, X. Shen, T. Yang, Y. Chen, C. Yan, *Adv. Mater.* **2017**, *29*, 1605160.

[13] Y. Fu, Z. Wu, Y. Yuan, P. Chen, L. Yu, L. Yuan, Q. Han, Y. Lan, W. Bai, E. Kan, C. Huang, X. Ouyang, X. Wang, J. Zhu, J. Lu, *Nat. Commun.* **2020**, *11*, 845.

[14] a) X. Wang, Z. Wang, L. Chen, *J. Power Sources* **2013**, *242*, 65; b) X. Zhou, Q. Liao, T. Bai, J. Yang, *J. Mater. Sci.* **2017**, *52*, 7719.

[15] H. Chen, G. Zhou, D. Boyle, J. Wan, H. Wang, D. Lin, D. Mackanic, Z. Zhang, S. C. Kim, H. R. Lee, H. Wang, W. Huang, Y. Ye, Y. Cui, *Matter* **2020**, *2*, 1605.

[16] a) Y. Jiang, Y. Deng, B. Zhang, W. Hua, X. Wang, Q. Qi, Q. Lin, W. Lv, *Nanoscale* **2020**, *12*, 12308; b) Y.-S. Su, A. Manthiram, *Nat. Commun.* **2012**, *3*, 1166; c) W. Kong, L. Yan, Y. Luo, D. Wang, K. Jiang, Q. Li, S. Fan, J. Wang, *Adv. Funct. Mater.* **2017**, *27*, 1606663.

[17] H. K. Lin, Y. L. Liu, *Macromol. Rapid Commun.* **2017**, *38*, 1700051.

[18] C. Velasco-Santos, A. L. Martinez-Hernandez, W. Brostow, V. M. Castaño, *J. Nanomater.* **2011**, *2011*, 928659.

[19] a) H. Yi, T. Lan, Y. Yang, Z. Lei, H. Zeng, T. Tang, C. Wang, Y. Deng, *J. Mater. Chem. A* **2018**, *6*, 18660; b) J. Pan, G. Xu, B. Ding, J. Han, H. Dou, X. Zhang, *RSC Adv.* **2015**, *5*, 13709; c) H. M. Kim, J. Y. Hwang, D. Aurbach, Y. K. Sun, *J. Phys. Chem. Lett.* **2017**, *8*, 5331; d) Y. Lu, Y. Jia, S. Zhao, L. Chen, Y. Su, F. Wu, J. Li, X. Liu, S. Chen, R. Chen, *ACS Appl. Energy Mater.* **2019**, *2*, 4151; e) G. Xu, Q.-b. Yan, A. Kushima, X. Zhang, J. Pan, J. Li, *Nano Energy* **2017**, *31*, 568; f) Z. Wang, Y. Dong, H. Li, Z. Zhao, H. B. Wu, C. Hao, S. Liu, J. Qiu, X. W. Lou, *Nat. Commun.* **2014**, *5*, 5002.

[20] a) Z.-J. Zhang, W. Cui, H. Xu, L. Xie, H. Liu, L.-M. Zhu, H. Li, R. Ran, *RSC Adv.* **2015**, *5*, 16604; b) G. Wu, S. Liu, X. Wu, X. Ding, *J. Appl. Polym. Sci.* **2017**, *134*, 44919; c) J. Zou, J. Liu, A. S. Karakoti, A. Kumar, D. Joung, Q. Li, S. I. Khondaker, S. Seal, L. Zhai, *ACS Nano* **2010**, *4*, 7293.

[21] a) J. Guo, K. Song, B. Wu, X. Zhu, B. Zhang, Y. Shi, *RSC Adv.* **2017**, *7*, 22875; b) S. R. Darmakkolla, H. Tran, A. Gupta, S. B. Rananavare, *RSC Adv.* **2016**, *6*, 93219; c) R. Yuan, P. Ju, Y. Wu, L. Ji, H. Li, L. Chen, H. Zhou, J. Chen, *J. Mater. Sci.* **2019**, *54*, 11069.

[22] a) J. Li, L. Han, D. Zhang, J. Li, T. Lu, X. Wang, L. Pan, *Inorg. Chem. Front.* **2019**, *6*, 2104; b) C. Hu, L. Lv, J. Xue, M. Ye, L. Wang, L. Qu, *Chem. Mater.* **2015**, *27*, 5253; c) J. Liu, T. Qian, M. Wang, X. Liu, N. Xu, Y. You, C. Yan, *Nano Lett.* **2017**, *17*, 5064.

[23] a) M. Cuisinier, P.-E. Cabelguen, S. Evers, G. He, M. Kolbeck, A. Garsuch, T. Bolin, M. Balasubramanian, L. F. Nazar, *J. Phys. Chem. Lett.* **2013**, *4*, 3227; b) Q. Pang, D. Kundu, M. Cuisinier, L. F. Nazar, *Nat. Commun.* **2014**, *5*, 4759.

[24] J. Pan, G. Xu, B. Ding, Z. Chang, A. Wang, H. Dou, X. Zhang, *RSC Adv.* **2016**, *6*, 40650.

[25] X. Zhao, M. Kim, Y. Liu, H.-J. Ahn, K.-W. Kim, K.-K. Cho, J.-H. Ahn, *Carbon* **2018**, *128*, 138.

[26] a) G. Zhou, E. Paek, G. S. Hwang, A. Manthiram, *Nat. Commun.* **2015**, *6*, 7760; b) F. He, J. Ye, Y. Cao, L. Xiao, H. Yang, X. Ai, *ACS Appl. Mater. Interfaces* **2017**, *9*, 11626; c) L.-C. Yin, J. Liang, G.-M. Zhou, F. Li, R. Saito, H.-M. Cheng, *Nano Energy* **2016**, *25*, 203; d) T. Z. Hou, W. T. Xu, X. Chen, H. J. Peng, J. Q. Huang, Q. Zhang, *Angew. Chem., Int. Ed. Engl.* **2017**, *56*, 8178.

[27] S. Kaewruang, P. Chiochan, N. Phattharasupakun, P. Suktha, K. Kongpatpanich, T. Maihom, J. Limtrakul, M. Sawangphruk, *Carbon* **2017**, *123*, 492.

[28] a) Q. Li, Y. Song, R. Xu, L. Zhang, J. Gao, Z. Xia, Z. Tian, N. Wei, M. H. Rümmeli, X. Zou, J. Sun, Z. Liu, *ACS Nano* **2018**, *12*, 10240; b) G. Zhou, E. Paek, G. S. Hwang, A. Manthiram, *Nat. Commun.* **2015**, *6*, 7760.

[29] a) Y. Guo, G. Zhao, N. Wu, Y. Zhang, M. Xiang, B. Wang, H. Liu, H. Wu, *ACS Appl. Mater. Interfaces* **2016**, *8*, 34185; b) H.-K. Kim, S.-M. Bak, S. W. Lee, M.-S. Kim, B. Park, S. C. Lee, Y. J. Choi, S. C. Jun, J. T. Han, K.-W. Nam, K. Y. Chung, J. Wang, J. Zhou, X.-Q. Yang, K. C. Roh, K.-B. Kim, *Energy Environ. Sci.* **2016**, *9*, 1270.

[30] Y. Yang, W. Sun, J. Zhang, X. Yue, Z. Wang, K. Sun, *Electrochim. Acta* **2016**, *209*, 691.

[31] J. Park, E. T. Kim, C. Kim, J. Pyun, H.-S. Jang, J. Shin, J. W. Choi, K. Char, Y.-E. Sung, *Adv. Energy Mater.* **2017**, *7*, 1700074.

[32] S. Wang, J. Liao, X. Yang, J. Liang, Q. Sun, J. Liang, F. Zhao, A. Koo, F. Kong, Y. Yao, X. Gao, M. Wu, S.-Z. Yang, R. Li, X. Sun, *Nano Energy* **2019**, *57*, 230.

[33] J. Wu, H. Zeng, X. Li, X. Xiang, Y. Liao, Z. Xue, Y. Ye, X. Xie, *Adv. Energy Mater.* **2018**, *8*, 1802430.

[34] Y. Luo, L. Wang, Z. Wei, Q. Huang, Y. Deng, Z. Zheng, *Adv. Energy Mater.* **2023**, *13*, 2203621.

[35] a) C. Xie, J. Chang, J. Shang, L. Wang, Y. Gao, Q. Huang, Z. Zheng, *Adv. Funct. Mater.* **2022**, *32*, 2203242; b) J. Chang, Q. Huang, Y. Gao, Z. Zheng, *Adv. Mater.* **2021**, *33*, 2004419; c) Y. Li, W. Huang, Y. Li, A. Pei, D. T. Boyle, Y. Cui, *Joule* **2018**, *2*, 2167; d) J. Shang, W. Yu, L. Wang, C. Xie, H. Xu, W. Wang, Q. Huang, Z. Zheng, *Adv. Mater.* **2023**, *35*, 2211748; e) J. Chang, H. Hu, J. Shang, R. Fang, D. Shou, C. Xie, Y. Gao, Y. Yang, Q. N. Zhuang, X. Lu, Y. K. Zhang, F. Li, Z. Zheng, *Small* **2022**, *18*, 2105308.

2400041 (11 of 11)